

Radiative Transfer Simulations of $\text{Ly}\alpha$ Intensity Mapping During Cosmic Reionization Including Sources from Galaxies and the Intergalactic Medium

Abigail E. Ambrose^a Eli Visbal^a Mihir Kulkarni^{a,b} Matthew McQuinn^c

^aRitter Astrophysical Research Center, University of Toledo, Dept. of Physics and Astronomy, 2801 West Bancroft Street Toledo, Ohio 43606, USA

^bInstitut für Astrophysik und Geophysik, Georg-August Universität Göttingen, Friedrich-Hund-Platz 1, D-37077 Göttingen, Germany

^cUniversity of Washington, Department of Astronomy, 3910 15th Avenue NE, Seattle, WA 98195, USA

E-mail: abigail.ambrose@rockets.utoledo.edu, mihir.kulkarni@uni-goettingen.de, elijah.visbal@utoledo.edu

Abstract. We present new simulations of Lyman- α ($\text{Ly}\alpha$) intensity maps that include $\text{Ly}\alpha$ radiative transfer in the intergalactic medium (IGM) and all significant sources of $\text{Ly}\alpha$ photons. The sources considered include $\text{Ly}\alpha$ directly from galaxies, cooling at the edges of ionized bubbles, recombinations within these bubbles, and reprocessing of galaxy continuum emission in the IGM. We also vary astrophysical parameters including the average neutral fraction of the IGM, the dust absorption of $\text{Ly}\alpha$ in galaxies, and the ionizing escape fraction. Previous work has suggested that $\text{Ly}\alpha$ intensity mapping can be used to constrain the neutral fraction of the IGM when accounting for radiative transfer in the IGM. When radiative transfer is ignored, direct $\text{Ly}\alpha$ emission from galaxies has the highest amplitude of power on all scales. When we include radiative transfer in our simulations, we find continuum emission reprocessed as $\text{Ly}\alpha$ is comparable to the $\text{Ly}\alpha$ emission directly from galaxies. For high neutral fraction in the IGM, emission from recombinations is comparable to galaxies on large scales. We find that the slope of the power spectrum is sensitive to the neutral fraction of the IGM when radiative transfer is included, suggesting that this may be useful for placing constraints on cosmic reionization. In addition, we find the power of galaxies is decreased across all scales due to dust absorption. We also find the escape fraction must be large for recombinations and bubble edges to contribute significantly to the power. We find the cross power is observable between SPHEREx and a hypothetical galaxy survey with a total signal-to-noise of 4 from $k = 0.035 \text{ Mpc}^{-1}$ to $k = 1 \text{ Mpc}^{-1}$.

Contents

1	Introduction	1
2	Methodology	2
2.1	21cmFAST Simulations	2
2.2	Ly α Photons from Galaxies	3
2.3	Edges of Ionized Bubbles	4
2.4	Recombinations in the Intergalactic Medium	5
2.5	Ultraviolet Continuum Emission from Galaxies	6
2.6	Ly α Radiative Transfer	8
3	Results	9
3.1	Sources of Ly α Photons	9
3.2	Astrophysical Parameter Effects	10
3.2.1	Effect of Neutral Fraction	10
3.2.2	Effect of Dust Absorption	11
3.2.3	Effect of Ionizing Photon Escape Fraction	12
3.3	Velocity Offset	12
3.4	Cross Correlation with a Galaxy Survey	14
4	Discussion and Conclusion	15

1 Introduction

The Epoch of Reionization (EoR) is an exciting frontier of research in cosmology. There have been many observations to constrain the properties of reionization. One of these observations is of the damping wing observed in the spectrum of galaxies and quasars, indicating that EoR ended as late as a redshift as $z \approx 5.3$. [1–4]. The Cosmic Microwave Background (CMB) indicates that the Universe was less than 10% reionized for redshifts $z > 10$ and that the midpoint of reionization occurred between a redshift of $z = 7.8$ and $z = 8.8$. Additionally, kinetic Sunyaev-Zeldovich (kSZ) effect measurements constrain the length of reionization to $\Delta z < 3$ [5]. Upcoming observations will allow us to tighten these constraints and gain a better understanding of reionization history and the sources driving it (see [6, 7] for recent reviews).

Intensity mapping is a promising new technique that could be used to probe cosmic reionization. This technique involves creating large-scale 3-dimensional (3D) maps of spectral line emission from galaxies and/or the intergalactic medium (IGM, [8, 9]). A key feature of these maps is they measure the combined emission from all sources including faint sources that are typically below the detection limit of traditional galaxy redshift surveys. A number of experiments have been proposed targeting a variety of lines such as Hydrogen Epoch of Reionization Array (HERA) mapping 21 cm emission, CO Mapping Array Project (COMAP) mapping CO emission, and CarBON CII line in post-reionization and ReionizaTiOn epoch (CONCERTO) mapping CII emission [10–12].

Future telescopes such as Spectro-Photometer for the History of the Universe, Epoch of Reionization and Ices Explorer (SPHEREx) and the proposed Cosmic Dawn Intensity

Mapper (CDIM) will be able to observe Lyman- α ($\text{Ly}\alpha$) during reionization [13–15]. $\text{Ly}\alpha$ will be a powerful line for this time period since it is a hydrogen recombination line, so no metals are necessary for these detections. The luminosity of $\text{Ly}\alpha$ is also dependent on the star formation rate (SFR) making it an excellent tracer for the cosmic star formation history (e.g. [16, 17]).

The authors of [18] suggested that $\text{Ly}\alpha$ intensity mapping would also constrain the timing of reionization because $\text{Ly}\alpha$ photons are easily scattered by the neutral IGM; however such radiative transfer was not included in previous models. This study showed that the $\text{Ly}\alpha$ power spectrum is sensitive to the global ionization fraction, small-scale power was suppressed for an increasing neutral fraction due to the smoothing of the signal from intergalactic scattering off of neutral regions. However, this work only focused on the signal from the galaxies and did not include other sources of $\text{Ly}\alpha$ photons.

In this paper, we model all significant sources of $\text{Ly}\alpha$ photons, including from galaxies, the edges of ionized bubbles, recombinations in the IGM, and reprocessing of galaxy continuum emission. We span a large parameter space in these simulations, including three different neutral fractions, four different values for dust absorption in galaxies, and three values for the escape fraction of ionizing photons. Finally, we forecast the cross-power of SPHEREx and a hypothetical galaxy survey in order to assess the detectability.

This paper is structured as follows. In Section 2 we discuss our simulations and the implementation of each source. In Section 3 we present our intensity maps, power spectra, and how different parameters effect these. Finally, in Section 4 we conclude with discussion of the implications of this work. Throughout this paper we assume Λ CDM with values $\Omega_m = 0.32$, $\Omega_\Lambda = 0.68$, $\Omega_b = 0.049$, and $h = 0.67$, consistent with the analysis in [19]. All cosmological distances are given in comoving units unless otherwise specified.

2 Methodology

In this section, we describe our methods for generating $\text{Ly}\alpha$ intensity maps. We utilize 21cmFAST [20], details of which can be found in Section 2.1. Then, we describe our modeling of the $\text{Ly}\alpha$ emission from all sources, including $\text{Ly}\alpha$ photons from galaxies, edges of ionized bubbles, recombinations in the IGM, and ultraviolet continuum emission from galaxies cascading down to $\text{Ly}\alpha$ photons in Sections 2.2–2.5. We describe our $\text{Ly}\alpha$ radiative transfer code in Section 2.6.

2.1 21cmFAST Simulations

We use the semi-numeric simulation 21cmFAST [20] to simulate the IGM density, the IGM neutral fraction, velocity field, and the halo density field. For the IGM density, initial conditions for the density and velocity are set and then the gravitational collapse is evolved according to first-order Lagrangian perturbation theory. Similarly, the velocity field is also given initial conditions and evolved following first-order perturbation theory. For the IGM neutral fraction, the fast Fourier radiative transfer (FFRT) method presented in [21] with an excursion-set approach is used to generate maps of HII regions using the density field. This method has been shown to reproduce the HII region distribution in full radiative transfer simulations of reionization [21]. The halo density field is created by finding overdensities in the IGM density that exceed the barrier for collapse in Sheth-Tormen [20, 22]. We set the minimum halo mass that hosts a galaxy to be $1.5 \times 10^9 M_\odot$ based on the analytic work of [23]. This analytic work as well as galaxy simulations, such as [24], shows that sources

down to $M_{\min} \approx 10^8 M_{\odot}$ can host star formation, but the efficiency is reduced by feedback below $10^9 M_{\odot}$.

We run these simulations for different values of cosmic neutral fraction and the ionizing escape fraction from galaxies. Our simulations are at a redshift of $z = 7$ with a size of $(200 \text{ Mpc})^3$ and a resolution of 256^3 voxels. Two astrophysical parameters in 21cmFAST also affect the properties of reionization including the maximum radius of an ionized region R_{\max} , and ionizing efficiency ζ . For all runs we use $R_{\max} = 50 \text{ Mpc}$, however, we note larger values would yield similar reionization morphology results. The ionizing efficiency is calculated as $\zeta = N_{\gamma} f_{\text{esc}} f_*$ where N_{γ} is the number of ionizing photons per stellar baryon, f_{esc} is the escape fraction of ionizing radiation as a function of halo mass, and f_* is the star formation efficiency as a function of halo mass. We will discuss how the escape fraction and star formation efficiency are determined in the following section.

2.2 Ly α Photons from Galaxies

For each galaxy in the simulation box, we assume the Ly α luminosity is proportional to the SFR similar to [18]. In addition, we include fraction of Ly α absorbed by dust, f_{dust} , use the star formation rate prescription from 21cmFAST, and allow the escape fraction of ionizing radiation, f_{esc} , to vary with halo mass. This results in a total Ly α luminosity from a galaxy of

$$L_{\text{gal}} = 2.0 \times 10^{42} (1 - f_{\text{esc}})(1 - f_{\text{dust}}) \frac{\dot{M}_*}{M_{\odot} \text{yr}^{-1}} \text{erg s}^{-1}, \quad (2.1)$$

where \dot{M}_* is the SFR of the galaxy. This equation assumes each ionization results in 0.6 Ly α photons and a Salpeter initial mass function [25].

Dust absorbs Ly α photons.¹ We allow the dust absorption fraction, f_{dust} , to vary as

$$f_{\text{dust}} = 1 - C_{\text{dust}} \times 10^{-3} (1 + z)^{\epsilon_{\text{dust}}}, \quad (2.2)$$

where C_{dust} and ϵ_{dust} are power-law coefficients calibrated to Ly α emitter observations in [17, 26], which gives us a fiducial value of $f_{\text{dust}} = 0.65$. However, there is considerable uncertainty in this parameter and so we will consider a range of values. We assume f_{esc} varies as

$$f_{\text{esc}} = f_{\text{esc},10} \left(\frac{m_{\text{h}}}{10^{10} M_{\odot}} \right)^{\alpha_{\text{esc}}}, \quad (2.3)$$

where $f_{\text{esc},10}$ is the escape fraction for a $10^{10} M_{\odot}$ halo, m_{h} is the halo mass, and α_{esc} is escape fraction power law [27] as used in 21cmFAST. The fiducial values we use for $f_{\text{esc},10}$ and α_{esc} are 0.1 and -0.5, respectively [27–30]. We calculate the SFR in a manner consistent with 21cmFAST where

$$\dot{M}_* = \frac{M_*}{t_* H(z)^{-1}}. \quad (2.4)$$

where t_* is a free parameter between zero and one, which we assume $t_* = 0.5$, $H(z)$ is the Hubble parameter, and the stellar mass of the galaxy is

$$M_* = f_* \frac{\Omega_{\text{b}}}{\Omega_{\text{m}}} m_{\text{h}}, \quad (2.5)$$

¹We assume that dust only absorbs Ly α photons and not continuum photons – while this is an extreme assumption, it is likely that the destruction of Ly α photons by dust is much larger because they scatter around the galaxy [17].

with f_* as the star formation efficiency. To compute this efficiency we use

$$f_* = f_{*,10} \left(\frac{m_h}{10^{10} M_\odot} \right)^{\alpha_*}, \quad (2.6)$$

where $f_{*,10}$ is the star formation efficiency for a fiducial $10^{10} M_\odot$ halo and α_* is the coefficient to the stellar baryon power law [27] as used in 21cmFAST. The fiducial values we use are $f_{*,10} = 0.0575$ (we include three significant figures here because the neutral fraction is sensitive to this value) and $\alpha_* = 0.5$ (see [27, 31, 32]), but we vary $f_{*,10}$ to set our ionizing efficiency. Our choices of α_* and α_{esc} result in an ionizing efficiency that is independent of halo mass.

To simplify the Ly α radiative transfer calculation, we apply a duty cycle to the galaxies so that only 10% of the galaxies are emitting Ly α at a given time, but they are 10 times brighter. We find this approximation has minimal effect on our results, as it increases of power on the smallest scales by a factor of 2. We model the emergent profile of the Ly α line from each galaxy to be a Gaussian with $1 - \sigma$ width of 100 km s^{-1} .

We also assume a redshifted velocity offset of 100 km s^{-1} to account for the effects of scattering in the interstellar medium (ISM), which is not resolved in our simulations. We include this because large amounts of scattering in the ISM results in an emergent spectrum sufficiently redshifted to allow photons to readily scatter to the observer and radiative transfer could be ignored. Alternatively, radiation could escape the galaxy by blueshifting instead, but redshifting has the potential to reduce the need for radiative transfer. We therefore focus on this portion of the spectrum and leave investigation of the exact emergent galaxy spectrum to future work. [33–35] show redshifted values for the velocity offset between 60 km s^{-1} and 250 km s^{-1} . We find that up to values of 500 km s^{-1} this velocity offset has little impact on our results, as discussed in Section 3.3.

2.3 Edges of Ionized Bubbles

The edges of ionized bubbles produce Ly α photons from collisional cooling of gas at the boundary of the ionized bubbles. Ionizing photons photoheat the gas which then cools along the edges of the ionizing bubbles as this region contains substantial ions and neutrals needed for efficient collisional cooling. This cooling primarily occurs via the emission of Ly α photons [17, 36–38]. The Ly α luminosity from these edges is approximately proportional to the number of ionizing photons produced by each halo.

Because of the proportionality between the number of ionizing photons produced by a halo and the luminosity of the edges, we find the Ly α luminosity for the edges by calculating the number of ionizing photons produced that escapes into the IGM. The number of ionizing photons is $N_{\text{ion},\gamma} = N_\gamma f_{\text{esc}} \dot{M}_* / m_p$, where $N_\gamma = 4000$ is the number of ionizing photons produced per baryon, and m_p is the mass of a proton. We then find the total Ly α luminosity of the edges to be the number of ionizing photons from the galaxy multiplied by the fraction of Ly α photons produced per ionization, $f_{\text{Ly}\alpha,\text{e}}$. We take into account the ionizing photons required to maintain ionization in HII regions with the factor f_{rec} given that recombinations continually occur throughout these ionized bubbles. This gives us

$$L_{\text{edges}} = N_\gamma f_{\text{Ly}\alpha,\text{e}} E_{\text{Ly}\alpha} f_{\text{esc}} (1 - f_{\text{rec}}) \frac{\dot{M}_*}{m_p}, \quad (2.7)$$

when summed over the SFRs of all halos. We will describe below how this is split into individual ionized bubbles. To get the number of Ly α photons produced by each ionization

we assume

$$f_{\text{Ly}\alpha, \text{e}} = \frac{(\epsilon - 3T_{\text{gas}}k_{\text{b}})}{10.2 \text{ eV}}, \quad (2.8)$$

where T_{gas} is the temperature the IGM gas cools to, which we assume to be 10,000 K (on the lower end of models which suggest $10^4 - 2.5 \times 10^4 \text{ K}$ [36]), and ϵ is the amount of heating per ionization. In order to calculate the heating per ionization we assume a specific flux $F_{\nu} \approx F_0 \nu^{-\alpha}$, where ν is the frequency of the light. F_0 and α are power law coefficients for galaxy flux and we assume $\alpha = 2$ for a stellar spectrum. We can then find the heating per ionization

$$\epsilon = \frac{\int_{\nu_0}^{4\nu_0} d\nu F_{\nu} (\nu - \nu_{\text{ion}})}{\int_{\nu_0}^{4\nu_0} d\nu F_{\nu}}, \quad (2.9)$$

where ν_{ion} is the frequency of a photon at the threshold for ionization and the integration limits ν_0 and $4\nu_0$ correspond to 1 Ry and 4 Ry as used in [36, 38]. This expression can be simplified to $\epsilon = 13.6 \text{ eV}/(\alpha - 1)$, if we assume contributions from helium are negligible, shown in [36]. This gives us a value of $f_{\text{Ly}\alpha, \text{e}} \approx 1.08$ for our assumptions, which is higher than the values between 0.2 and 0.8 found in [38], because of the lower value of T_{gas} we have assumed. We chose this lower value to bound the effect of ionization fraction emissions, which we find is likely to be subdominant even with our aggressive assumptions. We assume the IGM is sufficiently optically thick to use the case B recombination coefficient, α_{B} , although the difference between this assumption and case A can be absorbed into the uncertain clumping factor. The fraction due to recombinations can be approximated as

$$f_{\text{rec}} \approx C \alpha_{\text{B}} \bar{n}_{\text{H}}^2 (1 - x_{\text{HI}}) V_{\text{box}} / \dot{N}_{\text{ion, tot}}, \quad (2.10)$$

where $\dot{N}_{\text{ion, tot}}$ is the total number of ionizing photons ($N_{\text{ion}, \gamma}$) for all halos in the box, \bar{n}_{H} is the mean hydrogen number density of the universe, C is the clumping factor which we assume to be 5 [39–41], x_{HI} is the fraction of neutral hydrogen in a cell, and V_{box} is the volume of our simulation box in physical units. We assume the Ly α line shape from bubble wall emissions to be a Gaussian with thermal broadening, giving us a $1 - \sigma$ width of 90 km s^{-1} corresponding to $T_{\text{gas}} = 10^4 \text{ K}$. This thermal broadening is calculated as $\sqrt{k_{\text{b}} 10^4 (K) / m_{\text{p}}}$, where k_{b} is the Boltzmann constant.

In order to find the edges of ionized bubbles and the corresponding ionizing radiation strength, we perform a Monte Carlo ray tracing calculation. We achieve this by assigning each halo a number of rays proportional to its SFR to be emitted isotropically from each of the halos in our 21cmFAST outputs. Once the rays reach a neutral portion of the box we assume this to be the edge of an ionized bubble. Each ray divides the luminosity of Eq. 2.7 into discrete portions dependent on the halo’s SFR. We use 10^7 total rays to ensure our results are converged in our power spectrum out to a scale of $k = 1 \text{ Mpc}^{-1}$.

2.4 Recombinations in the Intergalactic Medium

We use the ionization fraction and density from 21cmFAST to calculate the Ly α flux from recombinations. The number density of hydrogen in each cell is given by $n_{\text{H}} = \bar{n}_{\text{H}}(1 + \delta)$ with δ being the overdensity of the cell given by the 21cmFAST simulations. We can then calculate the flux of a cell in our box due to Ly α from recombinations in the ionized bubbles in the IGM. We take the Ly α luminosity from recombinations to be

$$L_{\text{rec}} = V_{\text{cell}} C \alpha_{\text{B}} \bar{n}_{\text{H}}^2 (1 + \delta)^2 (1 - x_{\text{HI}}) f_{\text{Ly}\alpha, \text{r}} E_{\text{Ly}\alpha}, \quad (2.11)$$

where V_{cell} is the physical volume of a cell, x_{HI} is the hydrogen neutral fraction, $E_{\text{Ly}\alpha}$ is the energy of a Ly α photon, and $f_{\text{Ly}\alpha, \text{r}}$ is the fraction of the recombinations that will produce Ly α photons, which we assume to be 0.66 [42]. We assume the same Gaussian spectrum as we did for the edges of ionized bubbles in Section 2.3.

2.5 Ultraviolet Continuum Emission from Galaxies

An additional source of Ly α photons we consider are those produced by reprocessing of galaxy continuum emission in the IGM. As continuum emission photons leave a galaxy, some are redshifted into a Lyman series line and are absorbed in the IGM. This leads to cascading photons which have a certain probability to become Ly α photons depending on the Lyman series line where the absorption occurred. This physics is similar to Lyman-Werner feedback as it applies to the first stars [43–49]. The calculation we perform is similar to that of [48]. When we refer to an energy level, we are referring to the energy level the photon is absorbed before cascading to a Ly α photon.

These photons are reprocessed at redshift z_{rep} , which is given by

$$\frac{1 + z_{\text{rep}}}{1 + z_{\text{emit}}} = \frac{\nu_{\text{rep}}}{\nu_{\text{emit}}}, \quad (2.12)$$

where z_{emit} is the redshift of the galaxy, ν_{emit} is the frequency at which the continuum photon was emitted, and ν_{rep} is the Lyman series line in which the photon is reprocessed. This redshift can then be used to calculate the separation between the halo from which the photons were emitted and where they will be reabsorbed and cascade. We calculate this separation as

$$r = - \int_{z_{\text{rep}}}^{z_{\text{emit}}} c \frac{dz}{H(z)}, \quad (2.13)$$

where c is the speed of light. At $z > 6$, we can assume the matter-dominated case so the separation becomes

$$r = 2cH_0^{-1}\Omega_{\text{m}}^{-1/2}[(1 + z_{\text{rep}})^{-1/2} - (1 + z_{\text{emit}})^{-1/2}], \quad (2.14)$$

where H_0 is the Hubble constant. We assume the source galaxies have specific ultraviolet luminosity

$$L_{\nu} = a\dot{M}_{*} \left(\frac{\nu}{\nu_{\text{Ly}\alpha}} \right)^{-\alpha_{\text{UV}}}, \quad (2.15)$$

which we normalize so we have 9690 ultraviolet photons per baryon, based on the work by [50] and $\nu_{\text{Ly}\alpha}$ is the frequency of a Ly α photon. This gives us $a = 9.4637 \times 10^{27} \text{erg/s/Hz}$ when we use $\alpha_{\text{UV}} = 0.86$ as in [17] and is comparable to the values found in [51, 52]. Varying α_{UV} to match the average values in these works has little impact on our final results. We can then find the flux of a galaxy at the location where continuum photons are being reprocessed to be

$$F_{\nu} = \frac{L_{\nu}(\nu = \nu_{\text{emit}})}{4\pi D_{\text{L}}^2} \left(\frac{1 + z_{\text{emit}}}{1 + z_{\text{rep}}} \right) \exp[-\tau_{\nu}], \quad (2.16)$$

where τ_{ν} is the optical depth of that cell. We assume the optical depth is zero everywhere except for at the Lyman series lines, which we assume to be infinite. We can make this assumption because the optical depth of a Lyman series line is very high at line center at

relevant redshifts. This assumption is less accurate for $n > 3$, but these higher energy levels are a much smaller portion of the spectrum [53]. The luminosity distance D_L is given by

$$D_L \equiv \left(\frac{r}{1 + z_{\text{rep}}} \right) \left(\frac{1 + z_{\text{emit}}}{1 + z_{\text{rep}}} \right). \quad (2.17)$$

Using Eq. 2.16, we calculate the Ly α luminosity $L_{\text{Ly}\alpha, n}$ from continuum emission in each cell that are absorbed at energy level n before cascading to be

$$\begin{aligned} L_{\text{Ly}\alpha, n} &= \frac{E_{\text{Ly}\alpha}}{E_n} F_\nu f_{\text{Ly}\alpha, n} A_{\text{pixel}} \Delta\nu \\ &= \frac{\nu_{\text{Ly}\alpha}}{\nu_{\text{rep}}} \frac{L_\nu(\nu = \nu_{\text{emit}})}{4\pi} \left(\frac{1 + z_{\text{rep}}}{r} \right)^2 \left(\frac{1 + z_{\text{rep}}}{1 + z_{\text{emit}}} \right) f_{\text{Ly}\alpha, n} A_{\text{pixel}} \Delta\nu, \end{aligned} \quad (2.18)$$

where $f_{\text{Ly}\alpha, n}$ is the probability the photon will cascade into Ly α for each energy level, given by [54], A_{pixel} is the area of the pixel, E_n is the energy corresponding to energy level n , and $\Delta\nu$ is the frequency a photon would redshift across a cell a distance r away from the source if it was not absorbed at a Lyman-series line. The total luminosity from the continuum in a cell, L_{cont} , is the sum of Eq. 2.18 from $n = 2$ to $n = 30$. We only consider energy levels up to $n = 30$ as this yields convergent results in our luminosity. Note that Eq. 2.18 assumes we are working far from the source of the continuum.

When values of r are small, we must be more precise in our solution for finding the reprocessing to avoid unphysical solutions. To do this we perform a volume integral of Eq. 2.18. We find the equation for the luminosity $L_{\text{Ly}\alpha, n}$ of a cell to be

$$\begin{aligned} L_{\text{Ly}\alpha, n} &= \int_V \frac{E_{\text{Ly}\alpha}}{E_n} F_\nu f_{\text{Ly}\alpha, n} \frac{d\nu_{\text{emit}}}{dr} r^2 dr \sin\theta d\theta d\phi, \\ &= \frac{E_{\text{Ly}\alpha} f_{\text{Ly}\alpha, n}}{4\pi h} \frac{1}{(1 + z_{\text{emit}})} \int_V \frac{L_\nu(\nu_{\text{emit}})(1 + z_{\text{rep}})}{\nu_{\text{emit}}} \frac{d\nu_{\text{emit}}}{dr} dr \sin\theta d\theta d\phi, \end{aligned} \quad (2.19)$$

where h is Planck's constant. The bounds of this integral are the edge of the cell at a distance r from the originating halo. We solve this integral numerically for many distances from the originating halo and then sum over all energy levels. This gives us the total continuum luminosity of a single halo as a function of distance as shown in Figure 1.

To get the total continuum luminosity from all of the halos in the box we convolve the luminosity function onto each halo $L_{\text{cont, tot}} = L_{\text{Ly}\alpha} * \dot{M}_*$. We include periodic boundary conditions and the SFR is calculated the same way as was done in section 2.2.

The maximum distance that continuum photons travel from a given halo is 490 Mpc which exceed the size of our simulation box. This distance is set by how far a photon just outside of line center of $n = 3$ would travel to redshift into the line center of $n = 2$. In order to account for the continuum from halos outside the box we have to estimate their contribution. To do this we calculate the SFR in spherical shells with a radius greater than 100 Mpc (half the size of our simulation box). Within each spherical shell we estimate the abundance of halos of a given mass, dn/dM , using the Sheth-Tormen halo mass function [22]. We calculate the redshift of the shell using Eq. 2.14 solved for z_{emit} in order to calculate the mass function at that redshift. We then calculate the star formation rate density (SFRD),

$$\dot{\rho}_* = \int \frac{dn}{dM} \dot{M}_* dM. \quad (2.20)$$

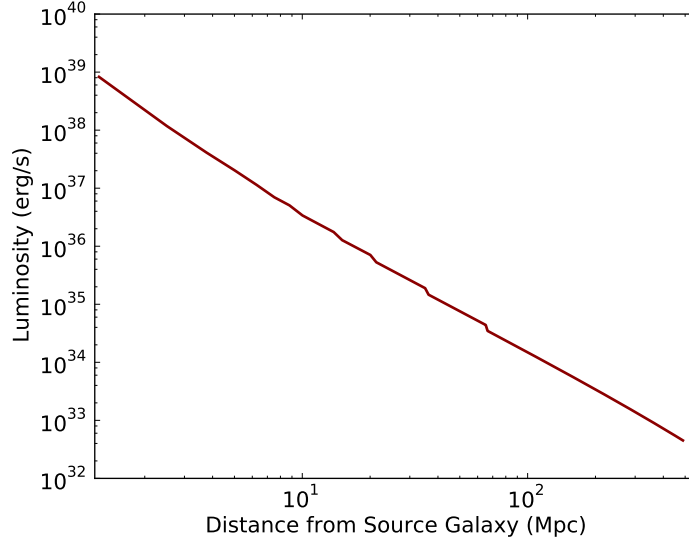


Figure 1. The $\text{Ly}\alpha$ luminosity in one of our simulation cells from the continuum as a function of distance from the source galaxy. The steps in this function are the result of the different distances associated with each energy level.

where the SFR is calculated in the same way as before. From this we can then calculate the SFR of the shells, $\dot{M}_{\text{shell}} = \dot{\rho}_* V_{\text{shell}}$, where V_{shell} is the volume of the spherical shell.

Using the SFR of each shell we can find the corresponding luminosity the shell deposits onto one cell, using the relationship in Eq. 2.19. We numerically integrate these shells to get the total luminosity deposited in a cell to be

$$L_{\text{hor}} = \int_{100 \text{ Mpc}}^{490 \text{ Mpc}} \dot{\rho}_* L(r_{\text{shell}}) 4\pi r^2 dr, \quad (2.21)$$

where $L(r_{\text{shell}})$ is normalized for SFR of $1\text{M}_{\odot}\text{yr}^{-1}$. This equation only includes $n = 2$ since this is the only Lyman series line that requires a distance of 100 Mpc or greater. We then apply this estimate to each cell in our simulation box so that we account for how the continuum emission from halos outside our simulation box affects the intensity map. We find this to be $\approx 40\%$ of the total continuum signal.

For our calculations, we assumed a Gaussian spectrum with thermal broadening for all components of the continuum. This spectrum used is the same as in Sections 2.3 and 2.4.

2.6 $\text{Ly}\alpha$ Radiative Transfer

The radiative transfer code we use is a Monte Carlo radiative transfer code similar to [55] and was used in [18] (see also [56–59]). We divide the luminosity of the sources into discrete photon packets. These photons will scatter and take a random walk in both frequency and position space until they escape the simulation box. At each scattering we determine the probability of a photon scattering to the observer and use this as the contribution to our intensity maps.

For each run we use three million photons. We check this convergence using the power spectra of the resulting intensity maps and find this many photons gives us convergence to a scale of $k = 1 \text{ Mpc}^{-1}$.

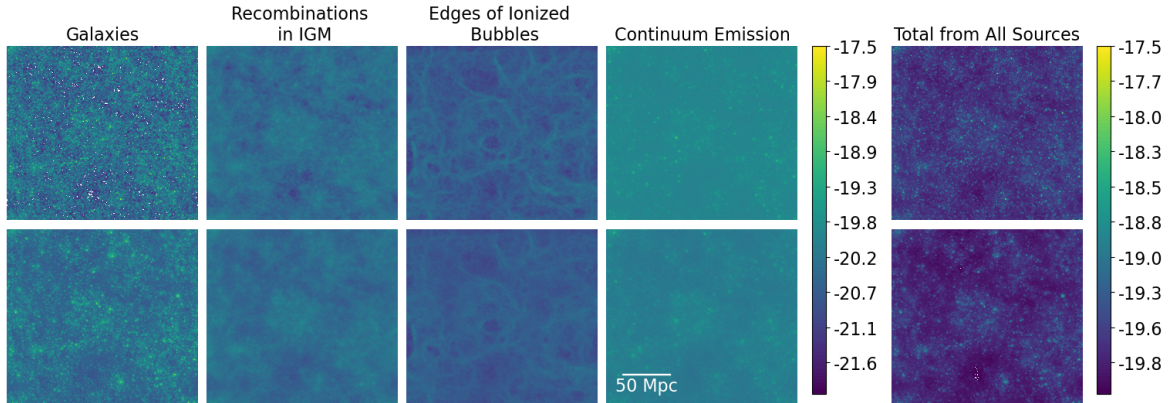


Figure 2. Intensity maps of each source with (bottom) and without (top) $\text{Ly}\alpha$ radiative transfer at $z = 7.0$, a neutral fraction of 0.50, escape fraction $f_{\text{esc},10} = 0.1$, dust absorption $f_{\text{dust}} = 0.65$. The right column shows the total from accounting for all four sources of $\text{Ly}\alpha$. The color bars are in units of $\log(\text{nWm}^{-2}\text{sr}^{-1})$ and the maps are 200 Mpc on each side.

3 Results

Here we present our simulated intensity maps as well as their associated power spectra. In Section 3.1 we show each source of $\text{Ly}\alpha$ photons. In Section 3.2 we show how different parameters effect the power spectra, including the neutral fraction, the fraction of $\text{Ly}\alpha$ absorbed by dust, and ionizing photon escape fraction. Our tested neutral fractions include $x_{\text{HI}} = 0.21, 0.5, 0.75$. Our dust models include $f_{\text{dust}} = 0.99, 0.65, 0.3$, and 0 for all three neutral fractions tested. Our models for escape fraction include $f_{\text{esc},10} = 0.1, 0.3$, and 0.8 with $x_{\text{HI}} = 0.5$. In Section 3.3, we show how various values for our velocity offset, used to approximate radiative transfer in the ISM, affects our simulation. In Section 3.4 we show a cross correlation between these intensity maps and a hypothetical galaxy survey alongside sensitivity curves for SPHEREx and a CDIM-like instrument. Our fiducial model has the parameters $z = 7.0$, $f_{\text{esc},10} = 0.1$, $x_{\text{HI}} = 0.5$, and $f_{\text{dust}} = 0.65$.

3.1 Sources of $\text{Ly}\alpha$ Photons

In Figure 2, we show the intensity maps for each source from our fiducial model before and after applying the $\text{Ly}\alpha$ radiative transfer. We see when we include $\text{Ly}\alpha$ radiative transfer the signal is smeared out. The maps are visually dominated by the continuum emission and $\text{Ly}\alpha$ photons from galaxies regardless of the inclusion of radiative transfer.

In Figure 3, we show the power spectra of the different $\text{Ly}\alpha$ sources for three different neutral fractions: 21%, 50% (fiducial), and 75%. The neutral fraction is dependent on the SFR and the escape fraction of ionizing radiation. In order to obtain these neutral fractions we changed the SFR of the galaxies by varying the star formation efficiency parameter $f_{*,10} = 0.07, 0.0575$, and 0.0375 for 21%, 50%, and 75%, respectively, while holding the escape fraction of ionizing radiation constant. The power of the galaxies and continuum decreases with decreasing SFR. The power of the recombinations and edges also decrease as the neutral fraction is increased due to the change in bubble volume and surface area, respectively.

In all panels of Figure 3, the $\text{Ly}\alpha$ photons directly from galaxies contribute the most power. The continuum emission, however, becomes comparable, particularly on large scales, to the galaxies when radiative transfer is included. Recombinations and edges have a lower

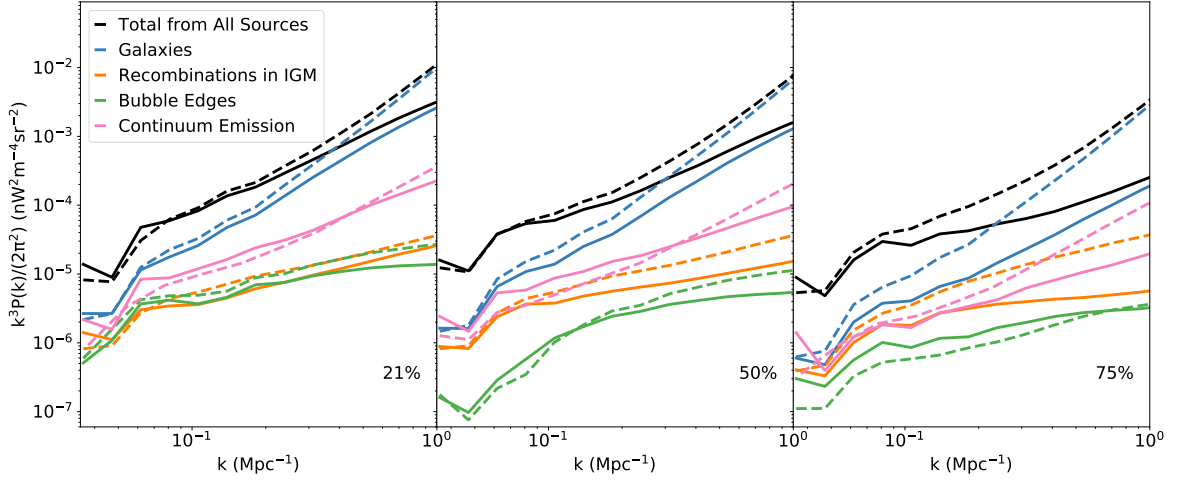


Figure 3. Power spectra for intensity maps with three different neutral fractions with $z = 7.0$, $f_{\text{esc},10} = 0.1$, and $f_{\text{dust}} = 0.65$. From left to right, the neutral fraction is 21%, 50%, and 75%. Solid and dashed lines respectively depict simulations with and without radiative transfer. The black is the total from all sources of Ly α , the blue is the Ly α emissions from galaxies, the orange is the Ly α from recombinations in the IGM, the green is the Ly α from cooling at the edges of ionized bubbles, and the pink is continuum emission cascading to Ly α photons. The radiative transfer has a large impact on the power spectrum, particularly on small scales, and has a larger impact the higher the neutral fraction of the IGM.

amplitude of power on all distance scales, regardless of radiative transfer. However, their relative contributions changes, varying with neutral fraction. We will discuss what parameters cause the power of the recombinations and edges to be higher than halos and continuum in following sections. It is important to note the total power spectrum is from taking the modulus squared of the sum of all contributions to the Ly α intensity, not the sum of the power spectra of the components (i.e. there are additional cross-power spectra that reflect correlations between the different Ly α sources).

3.2 Astrophysical Parameter Effects

In this section we examine how varying three different astrophysical parameters — the neutral fraction, the dust absorption in galaxies, and the ionizing photon escape fraction — affects our results. We also look at how this impacts the power of each source of Ly α photons.

3.2.1 Effect of Neutral Fraction

We show the total power spectra from all sources for our three neutral fractions in Figure 4. We can see that the neutral fraction has an effect on how much the slope of the power spectrum is decreased with radiative transfer. As shown in [18], Ly α radiative transfer smears out signal up to ≈ 10 Mpc. This smearing more heavily affects the signal on smaller scales causing a downward tilt in slope for our power spectra. For 21% neutral, $P_{\text{Ly}\alpha} \propto k^{-1.4}$. For 50% neutral, $P_{\text{Ly}\alpha} \propto k^{-1.7}$. For 75% neutral, $P_{\text{Ly}\alpha} \propto k^{-2.0}$. (Before radiative transfer 21% neutral $P_{\text{Ly}\alpha} \propto k^{-1.15}$, 50% $P_{\text{Ly}\alpha} \propto k^{-1.33}$, and 75% neutral $P_{\text{Ly}\alpha} \propto k^{-1.46}$.) All of these are fit $0.1 < k < 1.0$ Mpc with a least-squared fit. We chose to begin our fit at $k = 0.1$ to prevent the dip centered at $k \approx 0.05$ (from cosmic variance) affecting our fit. We cut off at $k = 1.0$ because this is where shot noise of Monte Carlo photons in our simulation

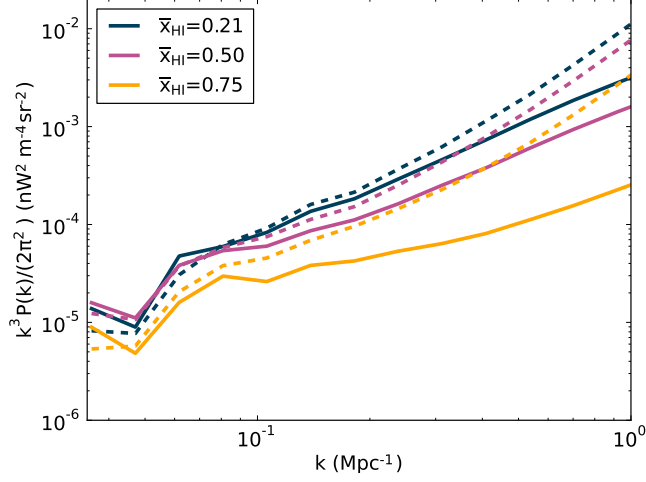


Figure 4. The impact of various neutral fractions on Ly α power spectrum. We show simulations with (solid) and without (dashed) including radiative transfer, for neutral fractions of 21% (navy), 50% (purple), and 75% (orange). Radiative transfer has a larger effect on the slope at higher neutral fractions.

is negligible. From Figure 4, we see that the slope is sensitive to the neutral fraction, even with all major sources of Ly α considered. We also note that for the fiducial model we find an amplitude of $P_{\text{Ly}\alpha} = 0.99 - 0.035 \text{ nW}^2 \text{ m}^{-4} \text{ sr}^{-2} \text{ Mpc}^3$ for $k \approx 0.1 - 0.9 \text{ Mpc}^{-1}$.

In Figure 4, we also see that on large scales the power is comparable between models with different neutral fractions. This is important because it shows how the power on such scales is relatively unaffected by changing SFR, so the slope is instead dependent on the neutral fraction. The uniform changing in power across distance scales is because the mean Ly α luminosity from galaxies and the continuum emission depends on the SFR.

We see some degeneracies between the slope changing due to the neutral fraction and the slope changing from other astrophysical parameters. We will discuss these degeneracies further in Sections 3.2.2 and 3.2.3.

3.2.2 Effect of Dust Absorption

We investigate the effect the fraction of Ly α photons absorbed by the dust in a galaxy has on our power spectra. As mentioned in Section 2.2, we assume that dust only absorbs Ly α photons and not continuum photons because of scattering of Ly α in the galaxy. Figure 5 shows the power spectra for the three different neutral fractions, with each panel showing different dust absorption fractions of 0, 0.3, 0.65 (fiducial model), and 0.99. The slope of the power spectra decreases with higher dust absorption because it suppresses power from galaxies while leaving the continuum emission unaffected. The continuum power spectrum is flatter than the galaxies, so larger contributions from the continuum result in a flatter power spectrum. We also see higher dust absorption results in suppression of power on all scales.

We note, we only see a substantial change in the slope from the highest value of dust absorption. For $x_{\text{HI}} = 0.5$ and $f_{\text{dust}} = 0$, $P_{\text{Ly}\alpha} \propto k^{-1.3}$, for $f_{\text{dust}} = 0.3$, $P_{\text{Ly}\alpha} \propto k^{-1.5}$, and for $f_{\text{dust}} = 0.99$, $P_{\text{Ly}\alpha} \propto k^{-2.1}$. We expect the neutral fraction to evolve more rapidly than the dust obscuration, so taking intensity maps over a few redshifts could disentangle this degeneracy and allow us to infer the neutral fraction from the power spectrum slope.

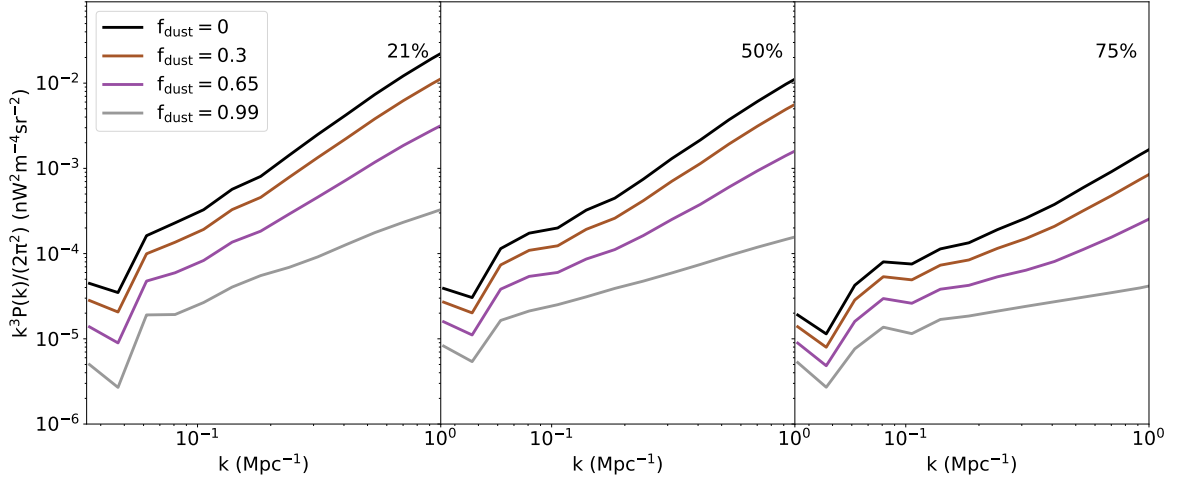


Figure 5. Power spectra for three different neutral fractions 21%, 50%, and 75% (left to right) with four different dust absorption fractions 0 (black), 0.3 (brown), 0.65 (purple, fiducial model), and 0.99 (gray). While dust absorption changes the slope of the total power spectra, this effect is subdominant to the effect of different neutral fractions.

3.2.3 Effect of Ionizing Photon Escape Fraction

The last parameter we vary in our models is the ionizing photon escape fraction. In Figure 6 we show the results with $f_{\text{esc},10} = 0.1, 0.3, \text{ and } 0.8$ with a neutral fraction $x_{\text{HI}} = 0.5$. In order to vary the escape fraction, while hold the neutral fraction constant, we vary our star formation efficiency parameters $f_{*,10} = 0.0575, 0.0192, \text{ and } 0.00719$ for $f_{\text{esc},10} = 0.1, 0.3, \text{ and } 0.8$ respectively. The amplitude of the power from each Ly α source depends on the escape fraction. For our lowest escape fraction, the galaxies and continuum have higher power than the other sources because the power for the galaxies proportional to $(1 - f_{\text{esc}})$ and the power for the edges and combinations proportional to f_{esc} . The highest escape fraction results in higher power from recombinations, followed by the bubble edges.

Figure 7 shows the total power spectra for the three different escape fraction values and a neutral fraction of 50%. The slope of the power decrease with increasing escape fraction. For $f_{\text{esc}} = 0.3$, $P_{\text{Ly}\alpha} \propto k^{-2.0}$ and for $f_{\text{esc}} = 0.8$, $P_{\text{Ly}\alpha} \propto k^{-2.3}$. We see the slope heavily affected by different values of the escape fraction. However, we believe that the neutral fraction would evolve much more rapidly, as was the case with dust absorption, so by taking intensity maps at multiple redshifts we could disentangle the degeneracy between these parameters. We save this calculation for future work.

3.3 Velocity Offset

Figure 8 shows how changing the velocity offset value for our galaxies alters the power spectra. We include this offset to approximate radiative transfer from the ISM which is not resolved in our simulations. We can see that there is minimal change in the power spectrum from including this velocity offset for values $< 500 \text{ km s}^{-1}$ as the photons are still close enough to the Ly α line to readily scatter. This shows radiative transfer in the ISM does not negate the need for including radiative transfer in the IGM for all values reported in [33–35]. If we instead include a symmetric profile of two Gaussians at $\pm 100 \text{ km/s}$ we will find a result comparable to that with no velocity offset.

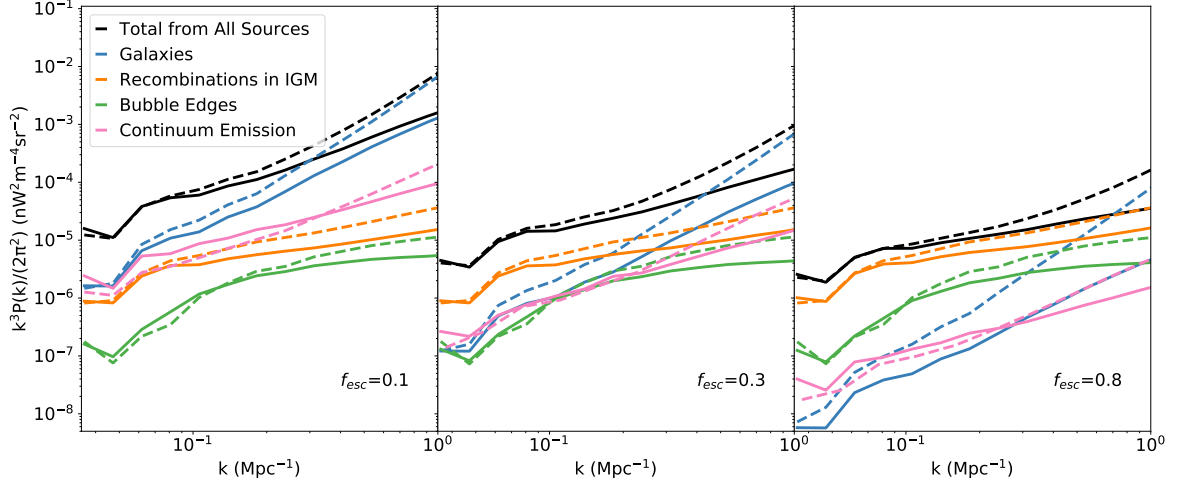


Figure 6. Power spectra for three different ionized photon escape fractions 0.1, 0.3, and 0.8 (left to right). The neutral fraction is held at $x_{\text{HI}} = 0.5$, which means we must decrease the SFR as we increase the escape fraction. Depending on the escape fraction, different sources of $\text{Ly}\alpha$ have higher amplitudes of power than others. For example, as we raise the escape fraction the recombinations and edges have higher amplitudes than the halos and continuum. The line style and colors on this plot are the same as in Fig. 3.

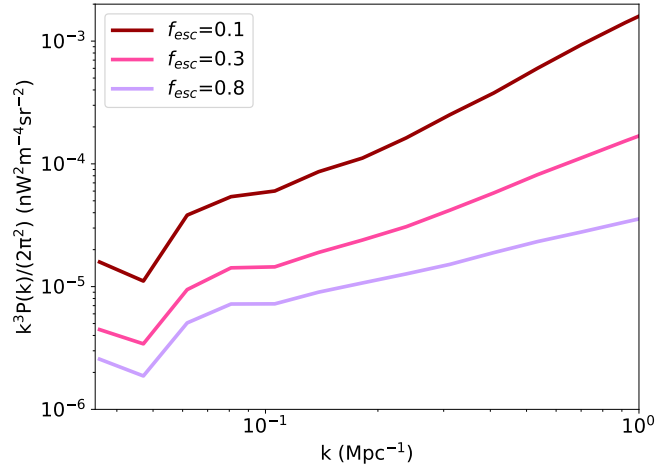


Figure 7. Total power spectra for the three different escape fractions with a neutral fraction $x_{\text{HI}} = 0.5$. We consider escape fractions of 0.1 (red), 0.3 (pink), and 0.8 (purple). Increasing the escape fraction decreases the slope of the power spectrum.

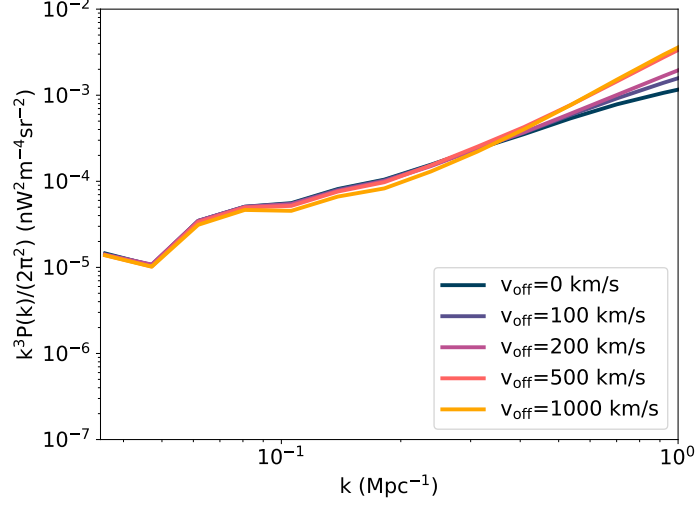


Figure 8. Power spectra for five different velocity offset values for the galaxies. The navy is 0 km/s, the purple is 100 km/s (fiducial), the pink is 200 km/s, the orange is 500 km/s, and the yellow is 1000 km/s. From this we can see there is a minimal deviation from our fiducial result, with more significant changes requiring offsets of > 500 km/s.

3.4 Cross Correlation with a Galaxy Survey

One of the main challenges to Ly α intensity mapping during reionization are interloping H α sources. Intensity maps of Ly α targeting $z = 7$ will contain foreground signal from H α emitting galaxies at $z \approx 0.5$. As a result, getting an auto power spectrum for Ly α will be challenging if not impossible [17]. For this reason, we investigate a cross correlation with a hypothetical galaxy survey in Figure 9. For this galaxy survey, we assume all galaxies with a mass $M_{\text{halo}} > 10^{11} M_{\odot}$ are observed. This gives us a volume density of $n_{\text{gal}} = 4.5 \times 10^{-4} \text{ Mpc}^{-3}$, similar to the *Subaru* Deep field narrow band survey at $z = 6.7$ [60], but would require more accurate redshift measurements than what is currently available for this data set. For this survey, we assume a $3^{\circ} \times 3^{\circ}$ field of view on the sky and $\Delta z = 0.5$ along the line of sight based on [61]; however, we note that this work covered $z = 6 - 6.574$ while our work is focused on $z = 7$. We use our 21cmFAST halo simulations in order to create synthetic galaxy redshift surveys with these specifications, and leave the investigation of more realistic surveys to future work. Our resulting fiducial model total power spans a dynamic range of $P_{\text{Ly}\alpha, \text{gal}} = 98.5 - 1.25 \text{ nWm}^{-2} \text{sr}^{-1} \text{Mpc}^{-3}$ for $k \approx 0.1 - 0.9 \text{ Mpc}^{-1}$.

In Figure 9, we also include sensitivity curves for SPHEREx and a CDIM-like telescope. For these, we find the error on the cross power to be

$$\delta P_{\text{Ly}\alpha, \text{gal}}(k)^2 = \frac{\frac{1}{2}(P_{\text{Ly}\alpha, \text{gal}}^2 + P_{\text{Ly}\alpha} P_{\text{gal}})}{N_k}, \quad (3.1)$$

where $P_{\text{Ly}\alpha, \text{gal}}$ is the cross power between our simulation and a hypothetical galaxy survey, P_{gal} is the auto power from this galaxy survey, N_k is the number of modes in a k -bin, and $P_{\text{Ly}\alpha}$ is the combination auto power from the simulation, noise power from SPHEREx or CDIM, and the power from the interloper H α , $P_{\text{Ly}\alpha} = P_{\text{auto, sim}} + P_{\text{N}} + P_{\text{H}\alpha}$.

For SPHEREx, we assume the noise power to be $P_{\text{N}} = \sigma_{\text{N}}^2 \Omega_{\text{pix}}$, where the instrument noise is assumed to be Gaussian with a variance of $\sigma_{\text{N}} = 3 \text{ nW m}^{-2} \text{sr}^{-1}$ and Ω_{pix} is the size of

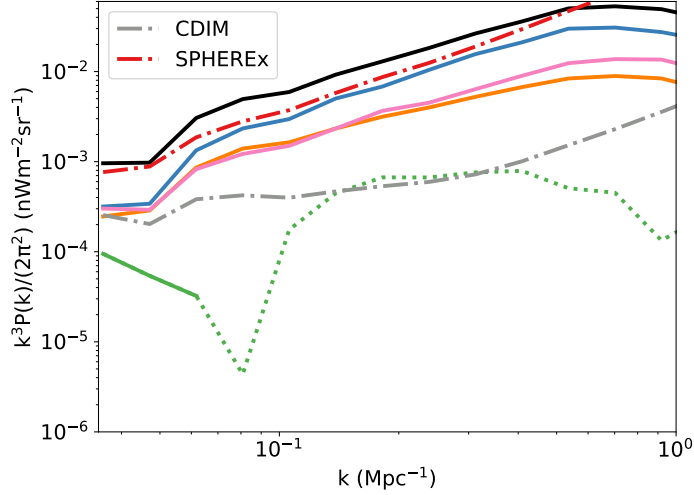


Figure 9. Cross power spectrum between our simulated intensity maps and a hypothetical galaxy survey. Line colors for the total, galaxies, continuum, recombinations, and edges power spectrum are the same as in Fig. 4. The dotting on the edges line indicates anticorrelation. The dot-dashed lines are sensitivity curves for SPHEREx (red) and a CDIM-like telescope (gray). These show that our total power will be observable with a total $S/N \approx 4$ for SPHEREx and $S/N \approx 12$ for CDIM.

a pixel for observations [13]. For a CDIM-like instrument, we assume 1.5 m telescope diameter and a spectral resolution of $R=300$ [15] and calculate the noise power in the same way as [62]. We also assume an integration time of 10^5 s, an observation efficiency from instrument losses of $\epsilon = 0.5$, and a zodiacal light background intensity of $\nu I_\nu = 500 \text{ nW m}^{-2} \text{ sr}^{-1}$ [17].

We find this observation is observable with SPHEREx up to $k \approx 0.8$, with a total signal-to-noise $S/N \approx 4$ from $k = 0.035 - 1 \text{ Mpc}^{-1}$ with bins $\Delta k = k/5$. The total signal-to-noise is $S/N = (\sum_k (P_{\text{Ly}\alpha, \text{gal}} / \delta P_{\text{Ly}\alpha, \text{gal}})^2)^{1/2}$. We only consider $k < 1 \text{ Mpc}^{-1}$ because this is when the shot noise of the Monte Carlo photons in our simulation are negligible. For CDIM, we find $S/N \approx 12$ across all modes from $k = 0.035 - 1 \text{ Mpc}^{-1}$ with bins $\Delta k = k/5$.

Figure 10 shows the cross power for this hypothetical galaxy survey with varying astrophysical parameters, including neutral fraction, dust absorption, and ionizing escape fraction. The trends we saw in the auto power spectra are still present, but are not as distinct. For example, the slope decreases with neutral fraction as it did in the auto power in Figure 4, but not to the same degree. The cross-power slope for each neutral fraction is $P_{\text{Ly}\alpha, \text{gal}} \propto k^{-1.5}$ for 21%, $P_{\text{Ly}\alpha, \text{gal}} \propto k^{-1.6}$ for 50%, and $P_{\text{Ly}\alpha, \text{gal}} \propto k^{-1.8}$ for 75%. We also see when looking at dust absorption, the slope of the power changes the most for the highest value of dust as we observed in Figure 5 and the amplitude of the cross power changes similar to the auto-power. We find a similar yet more significant trend for f_{esc} , in that the amplitude and slopes of both the auto and cross-power are decreased by increasing the escape fraction. The cross correlation is sensitive to models of reionization, but we defer full forecasting of these constraints to future work.

4 Discussion and Conclusion

We have simulated complete Ly α intensity maps during cosmic reionization including radiative transfer in the IGM. These simulations include Ly α photons from galaxies, the edges of

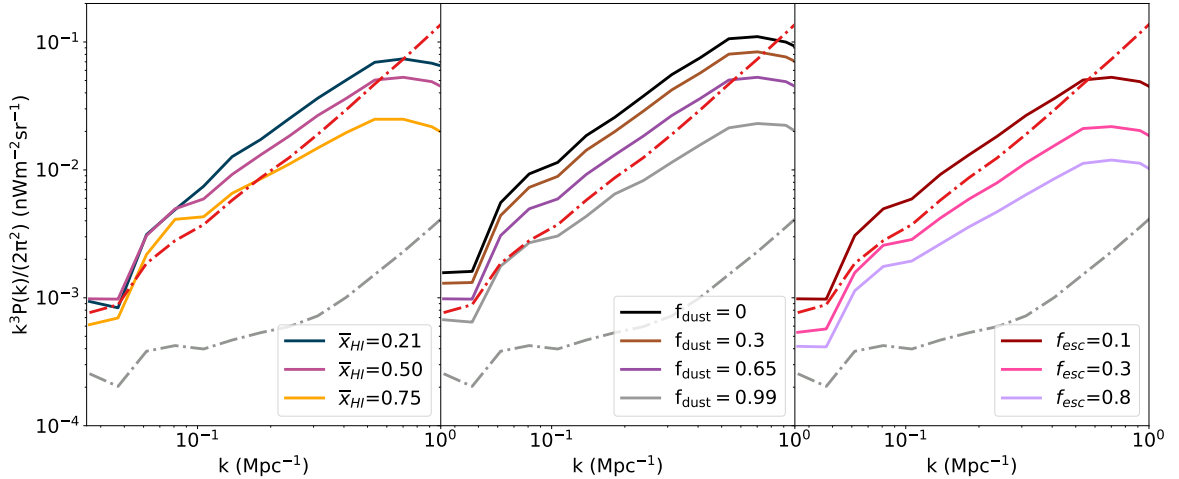


Figure 10. Cross power for each of the astrophysical parameters we varied with our hypothetical galaxy survey. From left to right the panels show the three neutral fractions, the four dust absorption fractions, and the ionizing escape fraction. The colors of this plot are the same as in other figures comparing these astrophysical parameter changes and the CDIM (gray) and SPHEREx (red) sensitivity curves the dot-dashed lines

ionized bubbles, recombinations in the IGM, and reprocessing of galaxy continuum emission. We also assessed the impact of three varying astrophysical parameters (neutral fraction, dust absorption, and ionizing escape fraction) on the intensity maps and associated power spectra.

We found the power spectra for our chosen Ly α sources vary in amplitude in response to a variety of factors including the neutral fraction of the IGM, the dust absorption in galaxies, and the escape fraction of ionizing photons. For our fiducial model, the galaxies and continuum are the strongest sources of fluctuations, while the edges and recombinations are negligible. We find that increasing neutral fractions result in higher power for the continuum and recombinations, while higher dust absorption results in a decrease in the galaxy power spectrum. Finally, we find that higher ionizing photon escape fractions result in the edges and recombinations power spectra to outweigh those of the galaxies and continuum. The contribution from galaxies is less than that of recombinations on the largest scales for $f_{\text{esc}} = 0.3$, and it becomes the least significant source at $f_{\text{esc}} = 0.8$.

We also found that the slope of the power spectrum can be used to infer the neutral fraction of the IGM, supporting the findings of [18]. We note the slope was impacted from varying the dust absorption and ionizing escape fraction, but these we believe these degeneracies have little effect on our ability to constrain the neutral fraction of the IGM. When observing over a range of redshifts, we expect to see less change in the dust absorption and ionizing escape fraction than we would for the neutral fraction, which would allow us to potentially disentangle these degeneracies. The neutral fraction may also be disentangled by using the fact that scattering by neutral gas leads to polarization [63].

We also investigated the effect of a velocity offset on the Ly α line from galaxies in order to approximate the radiative transfer in the ISM. We found that this velocity offset had little impact on the power spectra one would require an offset velocity of $v_{\text{off}} \geq 500$ km/s to significantly alter the power on the smallest scales, a value that is higher than those found in [33–35]. This indicates that radiative transfer in the IGM is a crucial component for such calculations.

Finally, using Ly α intensity maps from SPHEREx and a future galaxy redshift survey, we found the cross correlation signal will be detectable. We find a total S/N ≈ 4 for modes $k = 0.035 - 1 \text{ Mpc}^{-1}$. We also take cross correlations for power spectra with different astrophysical parameters. We see similar trends to those we saw previously in the auto-power, but less distinct.

In future work, we will perform a full analysis on the viability of constraining galaxy formation and reionization models with Ly α intensity mapping data using both auto and cross power. This will quantify in detail the degeneracies related to the dust absorption and ionizing escape fraction, as both values impact the slope of the power spectra in qualitatively similar ways.

Acknowledgments

The majority of our computations were carried out at the Ohio Supercomputer Center. EV is supported by NSF grant AST-2009309, NASA ATP grant 80NSSC22K0629, and STScI grant JWST-AR-05238. AA is supported by STScI grant JWST-AR-05238.

References

- [1] M. Iye, K. Ota, N. Kashikawa, H. Furusawa, T. Hashimoto, T. Hattori et al., *A galaxy at a redshift $z = 6.96$* , *Nature* **443** (2006) 186.
- [2] Y. Ono, M. Ouchi, B. Mobasher, M. Dickinson, K. Penner, K. Shimasaku et al., *Spectroscopic Confirmation of Three z -dropout Galaxies at $z = 6.844\text{--}7.213$: Demographics of Ly α Emission in $z \sim 7$ Galaxies*, *ApJ* **744** (2012) 83 [[1107.3159](#)].
- [3] M.A. Schenker, D.P. Stark, R.S. Ellis, B.E. Robertson, J.S. Dunlop, R.J. McLure et al., *Keck Spectroscopy of Faint $3 < z < 8$ Lyman Break Galaxies: Evidence for a Declining Fraction of Emission Line Sources in the Redshift Range $6 < z < 8$* , *ApJ* **744** (2012) 179 [[1107.1261](#)].
- [4] Y. Zhu, G.D. Becker, S.E.I. Bosman, C. Cain, L.C. Keating, F. Nasir et al., *Damping wing-like features in the stacked Ly α forest: Potential neutral hydrogen islands at $z < 6$* , *MNRAS* **533** (2024) L49 [[2405.12275](#)].
- [5] Planck Collaboration, Adam, R., Aghanim, N., Ashdown, M., Aumont, J., Baccigalupi, C. et al., *Planck intermediate results - xlvii. planck constraints on reionization history*, *A&A* **596** (2016) A108.
- [6] J.H. Wise, *Cosmic reionisation*, *Contemporary Physics* **60** (2019) 145 [<https://doi.org/10.1080/00107514.2019.1631548>].
- [7] B.E. Robertson, *Galaxy Formation and Reionization: Key Unknowns and Expected Breakthroughs by the James Webb Space Telescope*, *ARA&A* **60** (2022) 121 [[2110.13160](#)].
- [8] E. Visbal and A. Loeb, *Measuring the 3D clustering of undetected galaxies through cross correlation of their cumulative flux fluctuations from multiple spectral lines*, *JCAP* **2010** (2010) 016 [[1008.3178](#)].
- [9] J.L. Bernal and E.D. Kovetz, *Line-intensity mapping: theory review with a focus on star-formation lines*, *The Astronomy and Astrophysics Review* **30** (2022) 5.
- [10] D.R. DeBoer, A.R. Parsons, J.E. Aguirre, P. Alexander, Z.S. Ali, A.P. Beardsley et al., *Hydrogen epoch of reionization array (hera)*, *PASP* **129** (2017) 045001.
- [11] K.A. Cleary, J. Borowska, P.C. Breyse, M. Catha, D.T. Chung, S.E. Church et al., *Comap early science. i. overview*, *ApJ* **933** (2022) 182.

- [12] S. Dumitru, G. Kulkarni, G. Lagache and M.G. Haehnelt, *Predictions and sensitivity forecasts for reionization-era [C II] line intensity mapping*, *MNRAS* **485** (2019) 3486 [1802.04804].
- [13] Y.-T. Cheng and T.-C. Chang, *Cosmic near-infrared background tomography with sphereX using galaxy cross-correlations*, *ApJ* **925** (2022) 136.
- [14] F. Alibay, O.V. Sindiy, P.A.T. Jansma, C.M. Reynerson, E.B. Rice, J. Rocca et al., *SphereX preliminary mission overview*, in *2023 IEEE Aerospace Conference*, pp. 1–18, 2023, DOI.
- [15] A. Cooray, T.-C. Chang, S. Unwin, M. Zemcov, A. Coffey, P. Morrissey et al., *Cosmic Dawn Intensity Mapper*, in *Bulletin of the American Astronomical Society*, vol. 51, p. 23, Sept., 2019, DOI [1903.03144].
- [16] M.B. Silva, M.G. Santos, Y. Gong, A. Cooray and J. Bock, *Intensity Mapping of Ly α Emission during the Epoch of Reionization*, *ApJ* **763** (2013) 132 [1205.1493].
- [17] A.R. Pullen, O. Doré and J. Bock, *Intensity Mapping across Cosmic Times with the Ly α Line*, *ApJ* **786** (2014) 111 [1309.2295].
- [18] E. Visbal and M. McQuinn, *The Impact of Neutral Intergalactic Gas on Ly α Intensity Mapping during Reionization*, *ApJL* **863** (2018) L6 [1807.03370].
- [19] Planck Collaboration, Aghanim, N., Akrami, Y., Ashdown, M., Aumont, J., Baccigalupi, C. et al., *Planck 2018 results - vi. cosmological parameters*, *A&A* **641** (2020) A6.
- [20] A. Mesinger, S. Furlanetto and R. Cen, *21CMFAST: a fast, seminumerical simulation of the high-redshift 21-cm signal*, *MNRAS* **411** (2011) 955 [1003.3878].
- [21] O. Zahn, A. Lidz, M. McQuinn, S. Dutta, L. Hernquist, M. Zaldarriaga et al., *Simulations and Analytic Calculations of Bubble Growth during Hydrogen Reionization*, *ApJ* **654** (2007) 12 [astro-ph/0604177].
- [22] R.K. Sheth and G. Tormen, *Large-scale bias and the peak background split*, *MNRAS* **308** (1999) 119 [https://academic.oup.com/mnras/article-pdf/308/1/119/18409158/308-1-119.pdf].
- [23] S.R. Furlanetto, J. Mirocha, R.H. Mebane and G. Sun, *A minimalist feedback-regulated model for galaxy formation during the epoch of reionization*, *MNRAS* **472** (2017) 1576 [1611.01169].
- [24] J.Y.-C. Yeh, A. Smith, R. Kannan, E. Garaldi, M. Vogelsberger, J. Borrow et al., *The thesan project: ionizing escape fractions of reionization-era galaxies*, *MNRAS* **520** (2023) 2757.
- [25] D. Schaerer, *The transition from Population III to normal galaxies: Ly α and He II emission and the ionising properties of high redshift starburst galaxies*, *A&A* **397** (2003) 527 [astro-ph/0210462].
- [26] M. Hayes, D. Schaerer, G. Östlin, J.M. Mas-Hesse, H. Atek and D. Kunth, *On the Redshift Evolution of the Ly α Escape Fraction and the Dust Content of Galaxies*, *ApJ* **730** (2011) 8 [1010.4796].
- [27] J. Park, A. Mesinger, B. Greig and N. Gillet, *Inferring the astrophysics of reionization and cosmic dawn from galaxy luminosity functions and the 21-cm signal*, *MNRAS* **484** (2019) 933 [1809.08995].
- [28] H. Yajima, J.-H. Choi and K. Nagamine, *Escape fraction of ionizing photons from high-redshift galaxies in cosmological SPH simulations*, *MNRAS* **412** (2011) 411 [1002.3346].
- [29] A. Ferrara and A. Loeb, *Escape fraction of the ionizing radiation from starburst galaxies at high redshifts*, *MNRAS* **431** (2013) 2826 [1209.2123].
- [30] H. Xu, J.H. Wise, M.L. Norman, K. Ahn and B.W. O’Shea, *Galaxy Properties and UV Escape Fractions during the Epoch of Reionization: Results from the Renaissance Simulations*, *ApJ* **833** (2016) 84 [1604.07842].

- [31] P.S. Behroozi and J. Silk, *A Simple Technique for Predicting High-redshift Galaxy Evolution*, *ApJ* **799** (2015) 32 [[1404.5299](#)].
- [32] J. Mirocha, S.R. Furlanetto and G. Sun, *The global 21-cm signal in the context of the high- z galaxy luminosity function*, *MNRAS* **464** (2017) 1365 [[1607.00386](#)].
- [33] J. Blaizot, T. Garel, A. Verhamme, H. Katz, T. Kimm, L. Michel-Dansac et al., *Simulating the diversity of shapes of the Lyman- α line*, *MNRAS* **523** (2023) 3749 [[2305.10047](#)].
- [34] A. Smith, X. Ma, V. Bromm, S.L. Finkelstein, P.F. Hopkins, C.-A. Faucher-Giguère et al., *The physics of Lyman α escape from high-redshift galaxies*, *MNRAS* **484** (2019) 39 [[1810.08185](#)].
- [35] A. Smith, R. Kannan, S. Tacchella, M. Vogelsberger, L. Hernquist, F. Marinacci et al., *The physics of Lyman- α escape from disc-like galaxies*, *MNRAS* **517** (2022) 1 [[2111.13721](#)].
- [36] A. D’Aloisio, M. McQuinn, O. Maupin, F.B. Davies, H. Trac, S. Fuller et al., *Heating of the Intergalactic Medium by Hydrogen Reionization*, *ApJ* **874** (2019) 154 [[1807.09282](#)].
- [37] M.R. Santos, V. Bromm and M. Kamionkowski, *The contribution of the first stars to the cosmic infrared background*, *MNRAS* **336** (2002) 1082.
- [38] B. Wilson, A. D’Aloisio, G.D. Becker, C. Cain and E. Visbal, *Imaging reionization’s last phases with I-front Lyman- α emissions*, *JCAP* **2025** (2025) 066 [[2406.14625](#)].
- [39] I.T. Iliev, G. Mellema, P.R. Shapiro and U.-L. Pen, *Self-regulated reionization*, *MNRAS* **376** (2007) 534 [[astro-ph/0607517](#)].
- [40] M. McQuinn, A. Lidz, O. Zahn, S. Dutta, L. Hernquist and M. Zaldarriaga, *The morphology of H ii regions during reionization*, *MNRAS* **377** (2007) 1043.
- [41] A. D’Aloisio, M. McQuinn, H. Trac, C. Cain and A. Mesinger, *Hydrodynamic response of the intergalactic medium to reionization*, *ApJ* **898** (2020) 149.
- [42] D.E. Osterbrock and G.J. Ferland, *Astrophysics of gaseous nebulae and active galactic nuclei* (2006).
- [43] Z. Haiman, M.J. Rees and A. Loeb, *Destruction of molecular hydrogen during cosmological reionization*, *ApJ* **476** (1997) 458.
- [44] Z. Haiman, T. Abel and M.J. Rees, *The radiative feedback of the first cosmological objects*, *ApJ* **534** (2000) 11.
- [45] M.E. Machacek, G.L. Bryan and T. Abel, *Simulations of pregalactic structure formation with radiative feedback*, *ApJ* **548** (2001) 509.
- [46] J.H. Wise and T. Abel, *Suppression of H₂ cooling in the ultraviolet background*, *ApJ* **671** (2007) 1559.
- [47] B.W. O’Shea, J.H. Wise, H. Xu and M.L. Norman, *Probing the ultraviolet luminosity function of the earliest galaxies with the renaissance simulations*, *ApJ* **807** (2015) L12.
- [48] K. Ahn, P.R. Shapiro, I.T. Iliev, G. Mellema and U.-L. Pen, *The Inhomogeneous Background Of H₂-Dissociating Radiation During Cosmic Reionization*, *ApJ* **695** (2009) 1430 [[0807.2254](#)].
- [49] E. Visbal, Z. Haiman, B. Terrazas, G.L. Bryan and R. Barkana, *High-redshift star formation in a time-dependent Lyman–Werner background*, *MNRAS* **445** (2014) 107 [<https://academic.oup.com/mnras/article-pdf/445/1/107/18472155/stu1710.pdf>].
- [50] R. Barkana and A. Loeb, *Detecting the Earliest Galaxies through Two New Sources of 21 Centimeter Fluctuations*, *ApJ* **626** (2005) 1 [[astro-ph/0410129](#)].
- [51] J.S. Dunlop, R.J. McLure, B.E. Robertson, R.S. Ellis, D.P. Stark, M. Cirasuolo et al., *A critical analysis of the ultraviolet continuum slopes (β) of high-redshift galaxies: no evidence (yet) for extreme stellar populations at $z > 6$* , *MNRAS* **420** (2012) 901 [[1102.5005](#)].

- [52] F. Cullen, R.J. McLure, D.J. McLeod, J.S. Dunlop, C.T. Donnan, A.C. Carnall et al., *The ultraviolet continuum slopes (β) of galaxies at $z \simeq 8 - 16$ from jwst and ground-based near-infrared imaging*, *MNRAS* **520** (2023) 14.
- [53] J. Yang, F. Wang, X. Fan, J.F. Hennawi, F.B. Davies, M. Yue et al., *Measurements of the $z \sim 6$ Intergalactic Medium Optical Depth and Transmission Spikes Using a New $z > 6.3$ Quasar Sample*, *ApJ* **904** (2020) 26 [[2009.13544](#)].
- [54] C.M. Hirata, *Wouthuysen-Field coupling strength and application to high-redshift 21-cm radiation*, *MNRAS* **367** (2006) 259 [[astro-ph/0507102](#)].
- [55] C.-A. Faucher-Giguère, D. Kereš, M. Dijkstra, L. Hernquist and M. Zaldarriaga, *$Ly\alpha$ Cooling Emission from Galaxy Formation*, *ApJ* **725** (2010) 633 [[1005.3041](#)].
- [56] Z. Zheng and J. Miralda-Escudé, *Monte Carlo Simulation of $Ly\alpha$ Scattering and Application to Damped $Ly\alpha$ Systems*, *ApJ* **578** (2002) 33 [[astro-ph/0203287](#)].
- [57] S. Cantalupo, C. Porciani, S.J. Lilly and F. Miniati, *Fluorescent $Ly\alpha$ Emission from the High-Redshift Intergalactic Medium*, *ApJ* **628** (2005) 61 [[astro-ph/0504015](#)].
- [58] M. Dijkstra, Z. Haiman and M. Spaans, *$Ly\alpha$ Radiation from Collapsing Protogalaxies. I. Characteristics of the Emergent Spectrum*, *ApJ* **649** (2006) 14 [[astro-ph/0510407](#)].
- [59] P. Laursen and J. Sommer-Larsen, *$Ly\alpha$ Resonant Scattering in Young Galaxies: Predictions from Cosmological Simulations*, *ApJL* **657** (2007) L69 [[astro-ph/0610761](#)].
- [60] M. Ouchi, Y. Harikane, T. Shibuya, K. Shimasaku, Y. Taniguchi, A. Konno et al., *Systematic Identification of LAEs for Visible Exploration and Reionization Research Using Subaru HSC (SILVERRUSH). I. Program strategy and clustering properties of ~ 2000 $Ly\alpha$ emitters at $z = 6-7$ over the $0.3-0.5$ Gpc² survey area*, *PASJ* **70** (2018) S13 [[1704.07455](#)].
- [61] R. Higuchi, M. Ouchi, Y. Ono, T. Shibuya, J. Toshikawa, Y. Harikane et al., *Silverrush. vii. subaru/hsc identifications of protocluster candidates at $z \sim 6-7$: Implications for cosmic reionization*, *ApJ* **879** (2019) 28.
- [62] P. Comaschi and A. Ferrara, *Probing high-redshift galaxies with $Ly\alpha$ intensity mapping*, *MNRAS* **455** (2016) 725 [[1506.08838](#)].
- [63] L. Mas-Ribas and T.-C. Chang, *Lyman- α polarization intensity mapping*, *PhRvD* **101** (2020) 083032 [[2002.04107](#)].